

The Magnetic Structure of Individual Flux Vortices in Superconducting MgB_2 Derived using Transmission Electron Microscopy

J.C. Loudon,^{1,*} C.J. Bowell,^{1,†} N.D. Zhigadlo,² J. Karpinski,² and P.A. Midgley¹

¹*Department of Materials Science and Metallurgy, University of Cambridge,
Pembroke Street, Cambridge CB2 3QZ, United Kingdom*

²*Laboratory for Solid State Physics, ETH Zurich,
Schafmattstrasse 16, CH-8093, Zurich, Switzerland*

(Dated: May 23, 2018)

Images of flux vortices in superconductors acquired by transmission electron microscopy should allow a quantitative determination of their magnetic structure but so far, only visual comparisons have been made between experimental images and simulations. Here, we make a quantitative comparison between Fresnel images and simulations based on the modified London equation to investigate the magnetic structure of flux vortices in MgB_2 . This technique gives an absolute, low-field (~ 30 Oe) measurement of the penetration depth from images of single vortices. We found that these simulations gave a good fit to the experimental images and that if all the other parameters in the fit were known, the penetration depth for individual vortices could be measured with an accuracy of ± 5 nm. Averaging over 17 vortices gave a penetration depth of $\Lambda_{ab} = 113 \pm 2$ nm at 10.8 K assuming that the entire thickness of the sample was superconducting. The main uncertainty in this measurement was the proportion of the specimen which was superconducting. Allowing for a non-superconducting layer of up to 50 nm thickness on the specimen surfaces gave a penetration depth in the range $\Lambda_{ab} = 100\text{--}115$ nm, close to values of 90 ± 2 nm obtained by small-angle neutron scattering and $118\text{--}138$ nm obtained by radio-frequency measurements. We also discuss the use of the transport of intensity equation which should, in principle, give a model-independent measure of the magnetic structure of flux vortices.

PACS numbers: 74.25.Uv, 68.37.Lp

Keywords: MgB_2 , Flux vortices, Lorentz microscopy, Superconductivity.

I. INTRODUCTION

Superconductors expel magnetic flux from their interiors (the Meissner effect) but if a magnetic field is applied to a type-II superconductor which is larger than the lower critical field, H_{c1} , magnetic flux penetrates the superconductor by flowing along channels called flux vortices. Each vortex carries a single quantum of magnetic flux given by $\Phi_0 = h/2e$ where h is Planck's constant and e the electron charge. They consist of a core where superconductivity is suppressed with a radius given by the coherence length, ξ , surrounded by circulating supercurrents which persist over a radius given by the penetration depth, Λ . When flux vortices move, energy is lost and so the performance of almost all superconducting devices is determined by the behaviour of flux vortices.

Flux vortices can be imaged using transmission electron microscopy^{1,2} as shown in Fig. 1(a). The superconductor is thinned to about 250 nm so that it is electron-transparent and the flux vortices penetrate normal to the thin surface. It is mounted at a high angle, α (typically 45°), to provide a component of the B-field normal to the electron beam so that the electrons are deflected by the Lorentz force and appear as black-white features in an out-of-focus image. Electron microscopy is the only imaging technique which gives information on the internal magnetic structure of flux vortices, not just the stray fields, and it allows imaging at video rate. As we show here, it can be used to investigate the magnetic structure

of individual flux vortices and give an absolute measure of the penetration depth at low magnetic fields (typically 30 Oe) irrespective of whether the vortices form a regular array or not. Obtaining an absolute value for the penetration depth is important as it gives information on the number density of electrons involved in superconductivity³, the nature of the superconducting state⁴ and the types of vortex interaction which can occur⁵.

The ability to measure the magnetic properties of individual vortices is useful for the investigation of materials in which the vortices do not form a regular array: an effect which is hampering current research into some of the iron-based superconductors⁶. The technique would also provide a good method to test predictions that vortices containing non-integer multiples of the flux quantum should occur in 2-component superconductors such as MgB_2 when their size becomes comparable to the coherence length^{7,8}. It is also useful if the structure of certain vortices is altered by pinning as it would then be possible to see how the vortices respond to different types of pinning site. This type of experiment has been undertaken by Beleggia *et al.*⁹ but so far the only comparisons with theory have been visual. As shown in ref. 10, much of the information on the structure of the vortex is contained in the contrast of the image rather than its visual appearance. Here we use images of flux vortices taken from MgB_2 to make a quantitative comparison with simulations to assess how much information can be obtained using transmission electron microscopy. We first compare simulations of defocused images with those obtained ex-

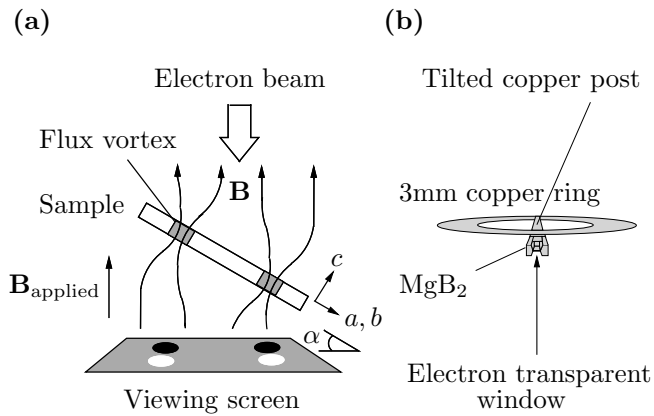


FIG. 1. (a) Experimental arrangement for imaging flux vortices. The electrons are deflected by the component of the B-field from the vortices normal to the electron beam giving a black-white feature in an out-of-focus image. (b) The specimen geometry. The MgB_2 specimen was mounted to a copper post glued to a standard 3 mm diameter copper ring at an angle of 45° . An electron transparent window was then cut by focussed ion-beam milling.

perimentally and then discuss the use the transport of intensity equation which in principle allows the magnetic structure of flux vortices to be derived directly from the experimental images.

II. MAGNESIUM DIBORIDE

MgB_2 was discovered to be a superconductor in 2001¹¹. It has a transition temperature $T_c = 39$ K and a hexagonal crystal structure (space group 191: $P6/mmm$) composed of alternating layers of magnesium and boron with lattice parameters $a = b = 3.086$ Å and $c = 3.542$ Å. It is an unusual superconductor as it has two sources of electrons which contribute to superconductivity: one associated with the σ bonding from the boron p_{xy} orbitals and the other associated with π bonding from the boron p_z orbitals. As a result, the penetration depth varies with the applied field as this changes the proportion of σ to π electrons contributing to superconductivity^{12,13}. In this experiment, the specimen was thinned to electron transparency in the c direction and since flux vortices penetrate parallel to the thin direction of the crystal, we make a low-field (~ 30 Oe) measurement of the penetration depth in the ab -plane, Λ_{ab} .

Only a few papers give values for the low-field penetration depth for MgB_2 resolved in crystallographic directions. Cubitt *et al.*¹³ use small-angle neutron scattering in which measurements were extrapolated to zero field (the lowest was made at 0.1 T) to give $\Lambda_{ab} = 82 \pm 2$ nm at 2 K. Very low field (~ 1 μT) radio-frequency measurements were also made by Manzano *et al.*¹⁴ giving $\Lambda_{ab} = 110$ –130 nm and $\Lambda_c = 210$ –280 nm and a coherence length $\xi_{ab} = 5.5$ nm as the temperature approaches

absolute zero. They also show that Λ_{ab} increases by 8.0 ± 1.6 nm as the temperature is increased from 1.35 K to 10.8 K, the temperature at which the experiments were conducted here.

III. METHODS FOR IMAGING FLUX VORTICES USING ELECTRON MICROSCOPY

As flux vortices are magnetic objects, they deflect but do not absorb the electron beam from the transmission electron microscope and so affect only the phase and not the intensity of the electron wavefunction. Consequently they are invisible in an in-focus image. There are two main imaging modes by which flux vortices can be visualised, giving access to the phase information. The first is off-axis holography¹⁵ where a positively charged wire (called an electron biprism) is placed beneath the specimen and used to interfere electrons which passed through the specimen with those which passed through vacuum to produce an interference pattern called a hologram. From this, the phase of the electron wavefunction can be calculated directly and differentiating the phase gives the B-field or more precisely, the induction-thickness product: the component of the B-field normal to the electron beam integrated along the path of the beam.

The other method is out-of-focus (also called Fresnel) imaging where images are taken out of focus and the vortices appear as black-white features¹. These can be compared with simulations or, if several images are taken at different defoci, the phase shift can be reconstructed using the transport of intensity equation but this is not as direct as holography as the intensity in a out-of-focus image is not sensitive to the phase or the phase gradient but only to the curvature and higher derivatives of the phase. As the induction-thickness product is proportional to the first derivative of the phase, this has the consequence that it can only be determined to within an additive constant. It might be thought, therefore, that off-axis holography would be the better method for investigating the structure of flux vortices as it gives a direct measurement of the phase shift but in fact, it has only been used to examine vortices in niobium by Bonevich *et al.*^{15,16}.

The main reason why out-of-focus imaging is the preferred method for investigating flux vortices lies in the way Shot noise in the image is transferred to noise in the recovered phase. In the Supplemental Information¹⁷ we show that if the m -th derivative of the phase is denoted $\phi^{(m)}$ then the noise associated with the phase derivatives recovered by holography is

$$\sigma_{\phi^{(m)}_{\text{holo}}} = \frac{1}{X^m} \sqrt{\frac{2^{m+1}}{NV^2}} \quad (1)$$

where N is the number of counts per reconstructed pixel, V is the visibility of the holographic fringes (the

difference between the maximum and minimum intensity divided by the sum) and X is the size of one pixel.

On the other hand, the noise associated with the phase derivatives obtained from Fresnel images is

$$\sigma_{\phi_{\text{Fresnel}}^{(m)}} = \frac{\pi}{X^{m-2}\lambda\Delta f} \sqrt{\frac{2^{m-1}}{N}} \quad (2)$$

Using reasonable values of $V = 30\%$, $N = 200$, $\lambda = 0.00197$ nm (the wavelength of 300 kV electrons) gives the noise in the curvature of the phase recovered by off-axis holography as $\sigma_{\phi_{\text{holo}}''} = 2.3$ mrad/nm² for the pixel size $X = 16.9$ nm used in this experiment. The noise can be reduced by increasing the pixel size and if $X = 50$ nm is used for the same number of electrons arriving at the detector, the noise is $\sigma_{\phi_{\text{holo}}''} = 0.09$ mrad/nm². This is close to the lowest resolution at which individual vortices can be resolved as the penetration depth of niobium is 52 nm.

Simulations for a 250 nm thick specimen tilted to $\alpha = 50^\circ$ give a maximum phase-curvature of 0.47 mrad/nm² for niobium (taking $\Lambda = 52$ nm [18]) and 0.12 mrad/nm² for MgB₂ (taking $\Lambda = 110$ nm) so it is clear that Bonevich *et al.* were working near to the limit of what is possible using electron holography, as they acknowledge¹⁶. We acquired electron holograms from MgB₂ and found that although the average B-field from the array of flux vortices could be observed, individual vortices could not be identified.

On the other hand, the noise expected in a phase reconstruction from defocused images is $\sigma_{\phi_{\text{Fresnel}}''} = 0.03$ mrad/nm² for $\Delta f = 1.1$ cm and $X = 16.9$ nm (used in this experiment) which is an improvement of 2 orders of magnitude compared with holography at the same resolution. This shows why out-of-focus imaging is the more commonly used method for imaging flux vortices. This mode of imaging is often referred to as ‘semi-quantitative’ but, as we show here, provided that the images are energy-filtered and recorded on a medium with a linear response, they contain all the information needed to make a quantitative comparison with simulations.

IV. EXPERIMENTAL METHODS

MgB₂ single crystals were synthesised by Dr J. Karpinski via the peritectic decomposition of MgNB₉ as described in ref. 19. The samples were thinned to 250 nm in the c -direction so that they were electron transparent using a Helios Nanolab dual-beam focussed ion beam microscope. To tilt the sample to a high angle (α in Fig. 1(a)), the specimen was mounted on a tilted copper post attached to a standard 3 mm copper ring as illustrated in Fig. 1(b).

Microscopy was undertaken using a Philips CM300 transmission electron microscope operated at 300 kV equipped with an electron biprism for holography, a

‘Lorentz’ lens and a Gatan imaging filter. The microscope was operated in low-magnification mode at a nominal magnification of 105 \times with the main objective lens turned off and the image was focussed with the diffraction lens. This proved more convenient than imaging with the Lorentz lens as a wider range of defoci could be accessed and in this mode, the selected area apertures become objective apertures and *vice versa* whereas in Lorentz mode, neither set of apertures is in the correct plane. The images were energy filtered so that only electrons which had lost 0–20 eV on passing through the specimen contributed to the image and an aperture was used so that only the 000 beam and the low-angle scattering from the vortices contributed to the image and the other crystallographic beams were excluded. The sample was cooled using a Gatan liquid-helium cooled ‘IKHCHDT3010-Special’ tilt-rotate holder which has a base temperature of 10 K.

The defocus and magnification were calibrated by acquiring images with the same lens settings as the original images from Agar Scientific’s ‘S106’ calibration specimen which consists of lines spaced by 463 nm ruled on an amorphous film. The defocus was found by taking digital Fourier transforms of the images acquired from the calibration specimen and measuring the radii of the dark rings which result from the contrast transfer function²⁰.

A thickness map of the specimen was created by dividing an unfiltered image by an energy-filtered image and taking the natural logarithm²¹ which gives the thickness parallel to the electron beam, l , as a multiple of the inelastic mean free path, λ_i . To determine λ_i , an electron hologram was taken at room temperature at an edge of the specimen which gives a phase shift proportional to the thickness, $\phi = C_E V_0 l$. C_E is a constant which depends only on the microscope voltage and has the value $6.523 \times 10^6 \text{ m}^{-1}\text{V}^{-1}$ at 300 kV. V_0 , the mean inner potential, was calculated as $V_0 = 17.71$ V from theoretical scattering factors given in ref. 22, giving $\lambda_i = 152 \pm 2$ nm and the thickness, l , varied from 330–400 nm across the field of view of Fig. 2(a). (Ideally the thickness of the whole specimen would have been determined by electron holography but the field of view of the interference region was not sufficiently large.)

V. COMPARISON OF DEFOCUSSED IMAGES WITH SIMULATIONS

We first compare defocused images with simulations based on the London model³ of flux vortices. The London model describes the B-field associated with a flux vortex but gives an unphysical divergence of the B-field as the centre of the vortex is approached. This is corrected by the Clem model²³ where the B-field profile is rounded near the centre of the vortex in a region called the vortex core which has a radius given by the coherence length, ξ . The London model should be a good approximation for MgB₂, however, as ξ_{ab} is about 6 nm whereas the

penetration depth is about 100 nm [14] and the pixel size of the images acquired here was 16.9 nm.

The phase shift, $\phi(x, y)$, an electron experiences on passing through a London vortex has been calculated by Beleggia and Pozzi²⁴ using a coordinate system in which the electron beam approaches the specimen in the z direction and x, y denote the image coordinates. It should be noted that their equation correctly accounts for the boundary conditions on the B-field at the interface between the superconductor and the vacuum so that the spreading of the B-field near the interface and the effect of the stray field are both contained in the model. If the intensity in the in-focus image is uniform over the field of view (a good approximation here since the in-focus intensity varies by about 5% over the size of each vortex image whereas the out-of-focus intensity varies by about 40% at the lowest defocus used here as can be seen from Fig. 2(c)), the in-focus electron wavefunction can be written as $\psi = e^{i\phi}$ and from this, any image which could be taken using the electron microscope can be simulated.

A defocused image can be simulated by using the Fresnel-Kirchoff integral²⁴ to propagate the in-focus electron wavefunction by a distance Δf , called the defocus. This is most easily accomplished by Fourier transforming the in-focus wavefunction in x and y but not z and multiplying by the phase factor $e^{-i\pi\Delta f\lambda k^2}$ (where λ is the electron wavelength and k the spatial frequency), inverse transforming and taking the square modulus. (Here and throughout we use the Fourier transform convention $\hat{f}(k) = \int_{-\infty}^{\infty} f(x)e^{-2\pi i k x} dx$.) It should be noted that under the conditions which vortices are imaged, the contribution from the spherical aberration of the lens is negligible. Here the diffraction lens was used to focus the image which has a spherical aberration coefficient of several metres but the coefficient would need to be $\sim 10^6$ m before the aberration and defocussing terms were comparable.

The variable parameters used to model the images were: the penetration depth Λ_{ab} , the position of the vortex in the image x, y , the thickness of superconducting material t , the tilting angle of the specimen α and the angle θ of the axis of the vortex as seen in the image. These were chosen to minimise the sum-square difference between the experimental and simulated images using the simplex algorithm given in ref. 25. A similar method was used to investigate the properties of pn junctions in semiconductors by Twitchett *et al.*²⁶.

The position of each vortex x, y and the rotation angle of the vortices θ given by the simplex algorithm are readily checked from the images. To give an independent measure of α , the angle between the plane of the copper ring and the specimen was measured in the focussed-ion beam microscope as $55 \pm 1^\circ$. However, in the electron microscope, the specimen was in shadow when the ring was horizontal and a tilt of -8.85° was required to reveal the electron transparent window. This would give $\alpha = 46^\circ$ if the axes of rotation were the same but since it is likely they were different by several degrees, α will

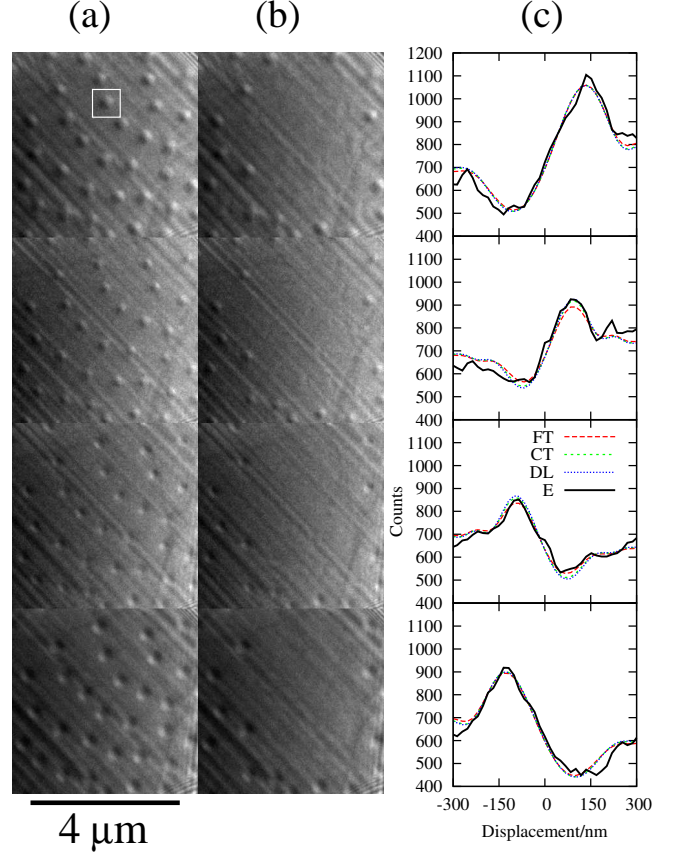


FIG. 2. (a) Defocus series taken in a field of 27 G at 10.8 K. The defoci are (top to bottom) $\Delta f = 2.24, 1.10, -1.10$ and -2.07 cm. (b) The same defocus series with simulated vortices subtracted for the case where all the variable parameters are optimised. The other fits mentioned in the text give very similar images. (c) Linescans at each defocus taken perpendicular to the axis of the vortex indicated by the white box in (a). FT: fitted thickness – simulation in which the thickness was used as a variable parameter giving $l = 543$ nm, $\alpha = 58^\circ$, $\Lambda_{ab} = 126$ nm. CT: calibrated thickness – simulation in which the thickness was fixed at its calibrated value, $l = 372$ nm, giving $\alpha = 51^\circ$, $\Lambda_{ab} = 107$ nm. DL: dead layer – simulation for which the thickness was fixed at $l = 300$ nm to mimic a dead-layer of non-superconducting material, giving $\alpha = 49^\circ$, $\Lambda_{ab} = 97$ nm. E – experimental data.

be larger and we estimate $\alpha = 50 \pm 5^\circ$.

The specimen thickness parallel to the electron beam, l , was measured to ± 2 nm using a combination of electron holography and energy-filtered imaging as explained in section IV. The thickness of the specimen parallel to the thin direction, t , is related to the thickness parallel to the electron beam, l , via $t = l \cos \alpha$ and the thicknesses quoted here are those parallel to the electron beam unless otherwise stated. This method gives the total thickness of the specimen but does not account for the possibility of ‘dead-layers’ of non-superconducting material produced by ion-beam thinning at the surface of the specimen. This is the largest of the uncertainties in this experiment

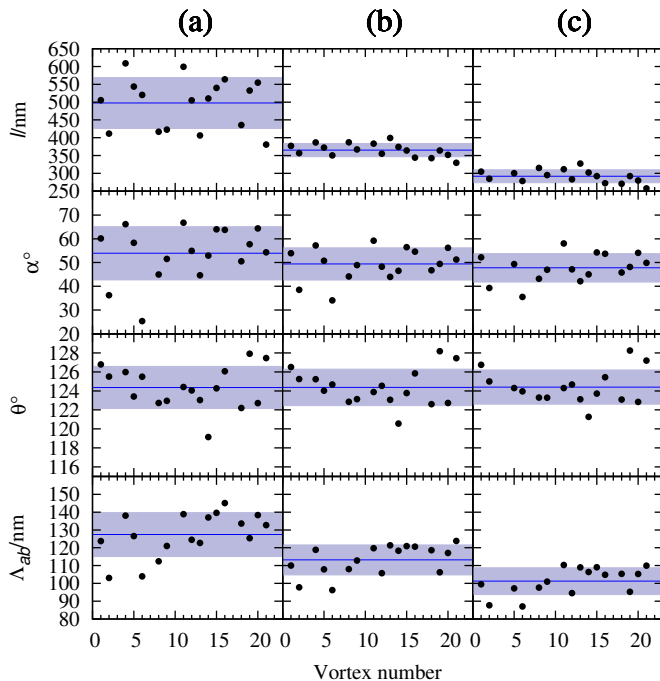


FIG. 3. Scatter graphs showing the results of the parameter optimisation generated by the simplex algorithm. In (a), the specimen thickness parallel to the electron beam, l , was treated as a variable parameter. In (b), it was fixed at its calibrated value. In (c), the thickness was reduced by 50 nm (72 nm parallel to the electron beam) from its calibrated value to simulate a ‘dead-layer’ of non-superconducting material. The horizontal line shows the mean and points within the shaded region are 1 standard deviation from the mean.

and its effect is discussed later.

We began by fitting all the parameters to the experimental data. Fig. 2(a) shows the defocus series and the black-white circular objects are the flux vortices. The diagonal stripes in the image are thickness undulations unintentionally introduced by focussed ion beam milling. As discussed in ref. 2 which used the same sample, they represent thickness undulations of about 1 nm. Vortices which were strongly affected by the contrast generated by these undulations were excluded from the fit. (b) shows the same images but where the fitted vortices have been subtracted. The fact that the vortices have been very effectively removed indicates that the fit is good. (c) shows linescans at each defocus taken perpendicular to the axis of a representative vortex indicated in (a) by the white box and it can be seen that there is a good match between simulation and experiment.

Fig. 3(a) shows scatter graphs of the optimal values of the parameters for each vortex. The mean penetration depth is $\Lambda_{ab} = 127$ nm and the standard deviation is 12 nm. There are no obvious outliers in the scatter graph so assuming that all the vortices have the same penetration depth gives $\Lambda_{ab} = 127 \pm 3$ nm.

To our surprise, the simplex algorithm gave thicknesses of superconducting material which were consid-

erably larger than the calibrated values. The average calibrated thickness was 365 nm but the average fitted thickness was 498 nm. We were expecting the fitted thicknesses to be shorter as there may have been damage introduced by the focussed ion beam milling resulting in non-superconducting material on the specimen surfaces. The problem seems to arise because the specimen tilt and the specimen thickness are to some extent complementary: if a vortex has a given projected length normal to the electron beam, this could be the result either of a thick specimen with a low tilt angle, α , or a thin specimen with a high tilt angle. The algorithm would then adjust the penetration depth to account for this.

To assess the extent to which a change in thickness changes the fitted penetration depth, we fixed the thicknesses at their calibrated values and re-ran the simplex algorithm. This resulted in Fig. 3(b) which gave a mean penetration depth of $\Lambda_{ab} = 113$ nm and a standard deviation of 8 nm so that $\Lambda_{ab} = 113 \pm 2$ nm. Fig. 2(c) shows that this change has almost no effect on the quality of the fit.

Finally we assess the effect of a dead-layer of non-superconducting material on the surfaces of the sample. In addition to measuring the total sample thickness via a combination of energy-filtered imaging and holography as described in section IV, we also took convergent-beam diffraction patterns from 5 regions of the sample under two-beam conditions. These were used to find the thickness of the crystalline component of the sample as described in ref. 20. The difference between the two measurements gives the thickness of any amorphous layers present but we found that to within the experimental error of ± 10 nm, there was no difference.

We repeated the simplex procedure with the superconducting thicknesses fixed at 50 nm (72 nm parallel to the electron beam) below their calibrated values which we consider to be the largest plausible dead-layer thickness. Again, Fig. 2(c) shows that the fit is still good and this yielded an average penetration depth of $\Lambda_{ab} = 101$ nm with a standard deviation of 8 nm. Averaging over all the vortices gives $\Lambda_{ab} = 101 \pm 2$ nm. Thus we can say that at 10.8 K, Λ_{ab} lies between 100–130 nm and is more likely to be between 100–115 nm.

VI. DERIVATION OF THE VORTEX STRUCTURE USING THE TRANSPORT OF INTENSITY EQUATION

In the previous section it was shown that simulated images based on the London model of flux vortices in MgB_2 provided a good fit to the experimental images. It would be advantageous, however, to derive the phase and the B-field from the images directly so that no aspects of the model are assumed. In principle, this can be done by reconstructing the phase from the defocussed images using the transport of intensity equation²⁷.

The transport of intensity equation is a re-expression

of the Schrödinger equation in terms of the intensity, I , and phase, ϕ , of the electrons combined with the condition that there is a constant flow of electrons. Using the same coordinate system as section V where the electron beam approaches the specimen in the z -direction, has wavelength λ and the image (located at $z = 0$) has coordinates x, y , the transport of intensity equation is:

$$\nabla_{xy} \cdot (I \nabla_{xy} \phi) = - \left(\frac{2\pi}{\lambda} \right) \frac{\partial I}{\partial z} \quad (3)$$

When the in-focus image has a uniform intensity, I_0 , (a good approximation for the images acquired here) the equation can be simplified to Poisson's equation:

$$\nabla_{xy}^2 \phi = - \left(\frac{2\pi}{\lambda I_0} \right) \frac{\partial I}{\partial z} \quad (4)$$

It can then be solved Fourier transforming in x and y but not z to give the Fourier transform of the phase as:

$$\tilde{\phi} = \frac{1}{2\pi\lambda I_0} \frac{1}{k^2} \text{F.T.} \left[\frac{\partial I}{\partial z} \right] \quad (5)$$

where F.T. stands for the Fourier transform of the term in square brackets. The rate of change of the intensity in the electron beam at the exit-plane of the specimen $z = 0$ may be estimated by taking two images with equal and opposite defocus, $\pm \Delta f$, so that $\frac{\partial I}{\partial z} \approx \frac{I(\Delta f) - I(-\Delta f)}{2\Delta f}$. The phase in real-space can then be found by calculating the inverse transform of Eqn. 5 numerically. The singularity at $k = 0$ in Eqn. 5 is indicative of the fact that the zero of phase is arbitrary so a constant can always be added without any physical consequences. Here the pixel at $k = 0$ was set to zero so the average phase in the image was zero. It can also be seen from Eqn. 4 that the recovered phase is not just insensitive to an additive constant but also to the addition of a phase ramp.

Ideally one would want to measure the B-field from the vortices. The quantity closest to this which can be derived from electron micrographs is the induction-thickness product, ' $(\mathbf{Bt})(x, y)$ ': the component of the B-field normal to the electron beam integrated along the length of the beam. It is related to the derivative of the phase via:

$$(\mathbf{Bt})(x, y) \equiv \int_{-\infty}^{\infty} \begin{pmatrix} B_x \\ B_y \end{pmatrix} dz = \frac{h}{2\pi e} \begin{pmatrix} -\partial\phi/\partial y \\ \partial\phi/\partial x \end{pmatrix} \quad (6)$$

For a conventional magnetic material where the B-field is constant through the thickness of the specimen and the stray field is negligible, the induction-thickness product is simply the component of the B-field normal to the electron beam multiplied by the thickness of the specimen. In the case of flux vortices, the stray field is not negligible and is included in the induction-thickness product. As

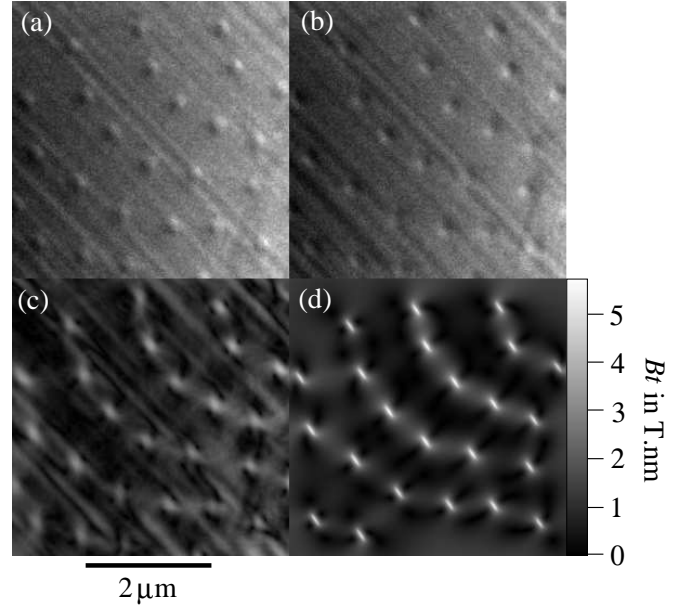


FIG. 4. (a) Original image taken with $\Delta f = 1.10 \pm 0.02$ cm. (b) Original image taken with $\Delta f = -1.10 \pm 0.02$ cm. (c) The magnitude of the induction-thickness product derived using the transport of intensity equation. (d) Simulated induction-thickness product for $\Lambda_{ab} = 113$ nm using the calibrated thicknesses.

mentioned above, the transport of intensity equation is insensitive to the addition of a phase ramp so the induction thickness product can only be recovered to within an additive constant. As the simulations were carried out with the same boundary conditions as the reconstructions, both have the same constant offset.

Fig. 4 shows two images, equally disposed either side of focus with $\Delta f = \pm 1.10$ cm. A longer defocus series was obtained but the transport of intensity equation works best for images closest to focus due to the approximation to the gradient of the intensity with defocus explained earlier. From these images, the modulus of the induction-thickness product shown in (c) was derived. (d) shows a simulation of the induction-thickness product for the same vortex array using $\Lambda_{ab} = 113$ nm and it can be seen that it is much more strongly peaked at the centre of the vortices. This could either indicate that the core of the vortices was much wider than previously thought or that the transport of intensity equation smooths the B-field profile.

To ascertain which of these possibilities was correct, we used the simulated phase shift to produce simulated defocused images and then applied the transport of intensity equation to these. Fig. 5(a) shows simulated profiles of the induction-thickness product across the centre of a vortex and it can be seen that it is indeed the use of the transport of intensity equation which broadens the B-field profiles. This effect is caused by subtracting two images close to focus to approximate the gradient $\frac{\partial I}{\partial z} \approx \frac{I(\Delta f) - I(-\Delta f)}{2\Delta f}$ and not by a lack of coherence in the

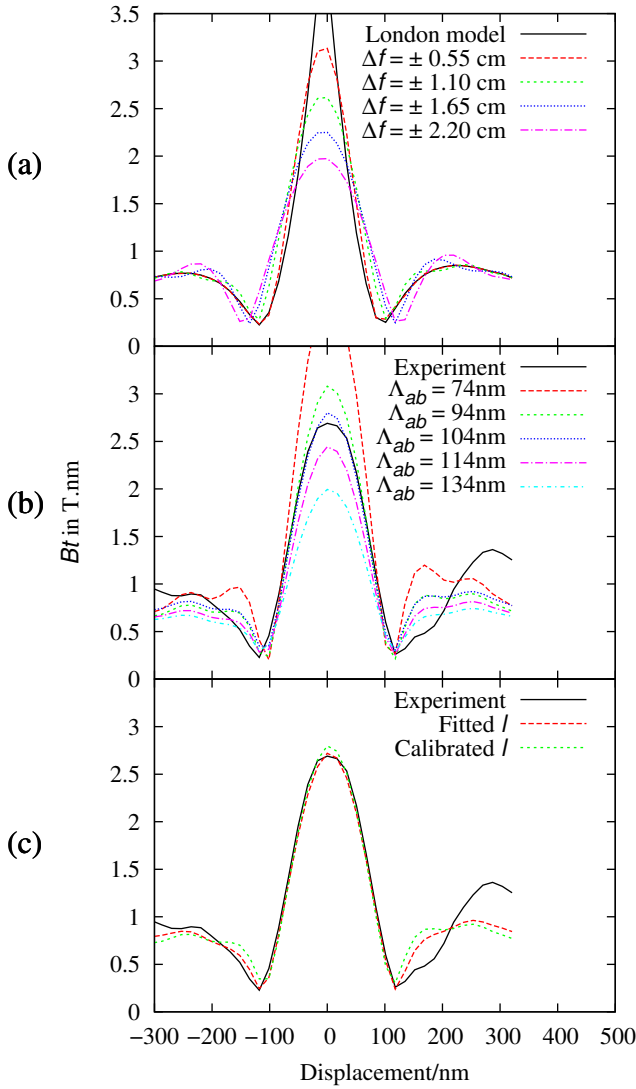


FIG. 5. (a) The modulus of the induction-thickness product (Bt) for a simulated London vortex (solid line) and reconstructions based on pairs of simulated images at the defoci shown. $\Delta f = \pm 1.10$ cm was used in this experiment. (b) Comparison of the induction-thickness product (Bt) reconstructed from experimental data for a single vortex with simulations for different values of Λ_{ab} . (c) Induction-thickness profile derived from experimental data using the transport of intensity equation together with simulated profiles. In the first, the thickness parallel to the electron beam was fitted as part of the simplex routine yielding $l = 530$ nm, $\alpha = 52^\circ$, $\Lambda_{ab} = 123$ nm. In the second simulation the thickness was fixed at the calibrated value of $l = 373$ nm, yielding $\alpha = 43^\circ$, $\Lambda_{ab} = 104$ nm.

electron beam as suggested in ref. 27.

Thus, the transport of intensity equation does not immediately yield the B-field profile of a flux vortex. To compare experiment and theory, it is first necessary to simulate defocused images from the theory and then generate a magnetic profile by applying the transport of intensity equation to these. Fig. 5(b) shows that when

this is done, a close match is obtained between the experimental profile and simulations based on the London model and that if the penetration depth were the only quantity subject to uncertainty, it would be possible to determine a best fit to within ± 5 nm.

As before, however, there is an ambiguity between the specimen thickness and the specimen tilt angle and Fig. 5(c) shows that very similar profiles can be obtained for different sets of parameters. The best values for the penetration depth were most likely found by direct comparison between experimental and simulated images in section V rather than the more convoluted process of applying the transport of intensity equation to experimental images and to simulated images and comparing the results. If this is done, however, it yields $\Lambda_{ab} = 125 \pm 4$ nm when the thickness is treated as a variable parameter and $\Lambda_{ab} = 112 \pm 3$ nm when the thicknesses are fixed at their calibrated values. As expected, these values are very similar to those obtained by comparing the experimental images with simulations in section V.

VII. SUMMARY AND CONCLUSIONS

Transmission electron microscopy gives a method to investigate the magnetic structure of individual flux vortices in type-II superconductors at low magnetic field and allows absolute measurements of the penetration depth to be obtained from individual vortices irrespective of whether they form a regular array. In section III we showed that out-of-focus imaging is a more sensitive method for measuring the B-fields associated with flux vortices compared with off-axis holography.

We investigated the magnetic structure of flux vortices in MgB_2 by comparing simulations based on the London model of flux vortices with out-of-focus images and found these gave a good fit indicating that the London model gives a good description of flux vortices in MgB_2 . The main uncertainty in the fits was the fraction of the sample thickness which was superconducting. Treating the thickness as a variable parameter in the fits and averaging over 17 vortices yielded a penetration depth of $\Lambda_{ab} = 127 \pm 3$ nm although this gave an implausibly large specimen thickness: an average of 498 nm as opposed to the calibrated average of 365 nm. Fixing the thicknesses at their calibrated values gave $\Lambda_{ab} = 113 \pm 2$ nm and reducing the thicknesses from their calibrated thicknesses by 50 nm to mimic a dead layer of non-superconducting material gave $\Lambda_{ab} = 101 \pm 2$ nm with only minimal changes to the goodness of fit. Thus at 10.8 K and in a field of 27 Oe, Λ_{ab} lies between 100–130 nm and is more likely to be between 100–115 nm.

The most reliable measurement of the penetration depth is likely to be the small-angle neutron scattering experiments from single crystals by Cubitt *et al.*¹³ which gave $\Lambda_{ab} = 82 \pm 2$ nm at 2 K. According to the radio-frequency measurements of Manzano *et al.*¹⁴, this will increase to 90 ± 2 nm at 10.8 K, the temperature

at which the measurements were made here. Although radio-frequency measurements are usually used to derive changes in the penetration depth, Manzano *et al.*¹⁴ were able to estimate absolute values of $\Lambda_{ab} = 110\text{--}130$ nm at 1.35 K which will increase to $\Lambda_{ab} = 118\text{--}138$ nm at 10.8 K using data from polycrystals and values for the anisotropy. Our values lie between these two measurements.

We also investigated the use of the transport of intensity equation which in principle allows the magnetic fields in the specimen to be derived without reference to a model. We found that although this gave a useful overview of the B-fields from the vortices, the B-field profiles are broadened due to the way the change of intensity with defocus is approximated. This must be taken into account when comparing the reconstructions with models so the technique does not provide a model-free method to determine the magnetic structure of vortices. It should be noted that if off-axis holography could be used, the magnetic profile would also be broadened due to the size of the Fourier mask used in the reconstruction process and this too would need to be accounted for.

The coherence length ξ_{ab} in MgB_2 is only 5.5 nm [14] and we did not observe any rounding of the B-field profile which could be ascribed to the coherence length. For a material with a larger coherence length like niobium, where the coherence length is 39 nm [18], observing the effect on the B-field profile should be quite feasible.

Quantitative measurements of the magnetic structure of flux vortices is only one aspect of the information which can be obtained using this technique. Information on the pinning landscape of the specimen can be derived from measurements of vortex motion²⁸ and we are currently preparing a paper on this subject.

ACKNOWLEDGMENTS

This work was funded by the Royal Society and the Engineering and Physical Sciences Research Council, Grant No. EP/E027903/1. Work at Eidgenössische Technische Hochschule Zurich was supported by the Swiss National Science Foundation and the National Centre of Competence in Research programme 'Materials with Novel Electronic Properties'.

VIII. SUPPLEMENTAL INFORMATION – THE EFFECT OF NOISE ON THE RECONSTRUCTED PHASE

Here we investigate how the noise in an image is transferred to the phase recovered from these images. The coordinate system is oriented so that the electron beam travels along z and the image lies in the xy -plane. For simplicity, we consider 1-dimensional images although the results can be readily extended to 2-dimensions. The

Fourier transforms referred to are taken in x and y but not z .

A. Noise in Phase Reconstructions from Holograms

Here we show how noise present in an off-axis hologram is transferred to the reconstructed phase. The standard expression²⁹ for the intensity in a hologram from a pure phase object is given by

$$I(x) = 1 + V \cos(2\pi Qx + \phi(x)) + n(x) \quad (7)$$

where V is the visibility of the holographic fringes, Q is the carrier frequency, $\phi(x)$ is the true phase shift (as opposed to that measured experimentally) and we have added noise, $n(x)$ which is the noise-to-signal ratio for each pixel (note that the average intensity per pixel has been normalised to 1). We now follow the usual procedure to reconstruct the phase from the hologram.

The first step is to take the Fourier transform of the intensity of the hologram which gives:

$$\begin{aligned} \tilde{I}(k) = & \delta(k) + \frac{V}{2} \left(\text{F.T.}[e^{i\phi(x)}] * \delta(k - Q) \right. \\ & \left. + \text{F.T.}[e^{-i\phi(x)}] * \delta(k + Q) \right) + \tilde{n}(k) \end{aligned} \quad (8)$$

where F.T. denotes the Fourier transform of the term in square brackets, $*$ is a convolution and $\tilde{n}(k)$ is the Fourier transform of the noise. It can be seen that the Fourier transform is composed of a central peak and two sidebands centred at $k = \pm Q$.

Next, the origin of the transform is shifted to the centre of the sideband at $k = Q$ by convolving both sides of the above equation by $\delta(k+Q)$. The sideband is then isolated by multiplying by a top hat function $\tilde{h}(k)$ which has the value 1 over the size of the sideband and is zero elsewhere to give a new function $\tilde{J}(k)$:

$$\tilde{J}(k) = \left(\frac{V}{2} \text{F.T.}[e^{i\phi(x)}] + \tilde{n}(k) * \delta(k + Q) \right) \tilde{h}(k) \quad (9)$$

The inverse transform gives:

$$J(x) = \left(\frac{V}{2} e^{i\phi(x)} + n(x) e^{2\pi i Qx} \right) * h(x) \quad (10)$$

It can be seen that in the absence of noise, $J(x)$ is proportional to the wavefunction of the electron beam as it exits the specimen, $e^{i\phi}$. The inverse transform of the top-hat function, $h(x)$, acts as a smoothing function and it controls the resolution of the reconstructed phase. Referring to the Argand diagram in Fig. 6, it can be seen that the phase measured by holography at a particular

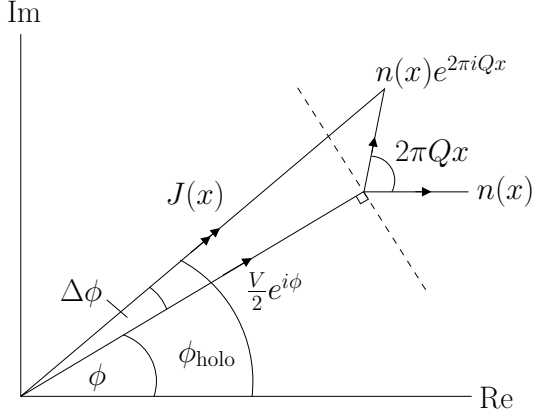


FIG. 6. Argand diagram showing the how noise in a hologram, $n(x)$, leads to noise $\Delta\phi$ in the recovered phase, ϕ .

position, x , is the sum of the true phase, ϕ and an additional phase due to the noise $\Delta\phi$ so that $\phi_{\text{holo}} = \phi + \Delta\phi$. The geometry of Fig. 6 shows that provided the noise-to-signal ratio is much smaller than the fringe visibility, $n/V \ll 1$, the additional phase shift is

$$\Delta\phi(x) = 2\frac{n(x)}{V} \sin(2\pi Qx - \phi(x)) \quad (11)$$

The noise in the phase recovered by holography is then the root-mean-square value of $\Delta\phi(x)$ averaged over the image. Denoting the average over the image by $\langle \rangle$, the noise in the phase image is

$$\sigma_{\phi_{\text{holo}}} \equiv \sqrt{\langle (\Delta\phi)^2 \rangle} = \sqrt{\frac{2}{V^2} \langle n^2(x) \rangle} = \sqrt{\frac{2}{NV^2}} \quad (12)$$

The last expression applies if the noise is Shot noise and there are N counts per pixel. It is the same as the formula given by Lichte *et al.*³⁰ although obtained by a different method.

Taking the m -th derivative (denoted by superscripts in brackets) of Eqn. 11 in the approximation that there are many pixels for each holographic fringe, $X \ll 1/Q$ gives

$$\phi_{\text{holo}}^{(m)}(x) = \phi^{(m)}(x) + 2\frac{n^{(m)}(x)}{V} \sin(2\pi Qx - \phi(x)) \quad (13)$$

The first derivative of the noise means the difference in the noise between two neighbouring pixels divided by the size of the pixel, X : $n'(x) = (n(x+X) - n(x))/X$. Subtracting the two noise terms from adjacent pixels increases the average noise by $\sqrt{2}$ and so the noise in the m -th derivative of the phase due to Shot noise in the original hologram is:

$$\sigma_{\phi_{\text{holo}}}^{(m)} = \frac{1}{X^m} \sqrt{\frac{2^{m+1}}{NV^2}} \quad (14)$$

B. Noise in Phase Reconstructions from Fresnel Images

Here we show how noise present in pairs of defocussed images is transferred to the phase recovered using the transport of intensity equation. The transport of intensity of equation is:

$$\nabla_{xy} \cdot (I \nabla_{xy} \phi) = - \left(\frac{2\pi}{\lambda} \right) \frac{\partial I}{\partial z} \quad (15)$$

For a phase object with unit average intensity, this simplifies to

$$\nabla_{xy}^2 \phi = - \left(\frac{2\pi}{\lambda} \right) \frac{\partial I}{\partial z} \quad (16)$$

The derivative is found from two images equally disposed either side of focus so that

$$\nabla_{xy}^2 \phi = - \left(\frac{2\pi}{\lambda} \right) \frac{I(\Delta f) - I(-\Delta f)}{2\Delta f} \quad (17)$$

If I denotes the ideal intensity of the image and I_{expt} is the intensity measured experimentally subject to a noise-to-signal ratio at each pixel of $n(x, y)$, we have

$$I_{\text{expt}}(\Delta f) = I(\Delta f) + n(\Delta f) \quad (18)$$

and

$$I_{\text{expt}}(-\Delta f) = I(-\Delta f) + n(-\Delta f) \quad (19)$$

Giving

$$\nabla_{xy}^2 \phi_{\text{Fresnel}} = \nabla_{xy}^2 \phi - \frac{\pi}{\lambda \Delta f} (n(\Delta f) - n(-\Delta f)) \quad (20)$$

As in the previous section, subtracting the two noise terms increases the average noise by a factor of $\sqrt{2}$ so the noise in the m -th derivative of the phase recovered by the transport of intensity equation from images with an average count of N electrons per pixel and subject to Shot noise is

$$\sigma_{\phi_{\text{Fresnel}}}^{(m)} = \frac{\pi}{X^{m-2} \lambda \Delta f} \sqrt{\frac{2^{m-1}}{N}} \quad (21)$$

ACKNOWLEDGMENTS

This work was funded by the Royal Society and the EPSRC, Grant No. EP/E027903/1. Work at ETH was supported by the SNSF and the NCCR program MaNEP.

-
- * j.c.loudon@gmail.com
- † Now at Integrated Plasmonics, 2122 Bryant Street, San Francisco, CA 94110, USA.
- ¹ K. Harada, T. Matsuda, J. Bonevich, M. Igarashi, S. Kondo, G. Pozzi, U. Kawabe, and A. Tonomura, *Nature* **360**, 51 (1992).
 - ² J. C. Loudon, C. J. Howell, N. D. Zhigadlo, J. Karpinski, and P. A. Midgley, *Physica C* **474**, 18 (2012).
 - ³ M. Tinkham, *Introduction to Superconductivity*, 2nd edn. (Dover Publications Inc., Mineola, 1996).
 - ⁴ V. Moshchalkov, M. Menghini, T. Nishio, Q. H. Chen, A. V. Silhanek, V. H. Dao, L. F. Chibotaru, N. D. Zhigadlo, and J. Karpinski, *Phys. Rev. Lett.* **102**, 117001 (2009).
 - ⁵ A. Chaves, L. Komendová, M. V. Milošević, J. S. Andrade Jr., G. A. Farias, and F. M. Peeters, *Phys. Rev. B* **83**, 214523 (2011).
 - ⁶ M. R. Eskildsen, *Front. Phys.* **6**, 398 (2011).
 - ⁷ L. F. Chibotaru and V. H. Dao, *Phys. Rev. B* **81**, 020502 (2010).
 - ⁸ R. Geurts, M. V. Milošević, and F. M. Peeters, *Phys. Rev. B* **81**, 214514 (2010).
 - ⁹ M. Beleggia, G. Pozzi, J. Masuko, N. Osakabe, K. Harada, T. Yoshida, O. Kamimura, H. Kasai, T. Matsuda, and A. Tonomura, *Phys. Rev. B* **66**, 174518 (2002).
 - ¹⁰ J. C. Loudon and P. A. Midgley, *Ultramicroscopy* **109**, 700 (2009).
 - ¹¹ J. Nagamatsu, N. Nakagawa, T. Kuranaka, Y. Zenitani, and J. Akimitsu, *Nature* **410**, 63 (2001).
 - ¹² M. Karmakar and B. Dey, *J. Phys.: Condens. Matter* **22**, 205701 (2010).
 - ¹³ R. Cubitt, M. R. Eskildsen, C. D. Dewhurst, J. Jun, S. M. Kazakov, and J. Karpinski, *Phys. Rev. Lett.* **91**, 047002 (2003).
 - ¹⁴ F. Manzano, A. Carrington, N. E. Hussey, S. Lee, A. Yamamoto, and S. Tajima, *Phys. Rev. Lett.* **88**, 047002 (2002).
 - ¹⁵ J. Bonevich, G. Pozzi, and A. Tonomura, in *Introduction to Electron Holography*, edited by E. Völkl, L. Allard, and D. Joy (Kluwer Academic, New York, 1999) Chap. 7, pp. 153–181.
 - ¹⁶ J. E. Bonevich, K. Harada, T. Matsuda, H. Kasai, T. Yoshida, G. Pozzi, and A. Tonomura, *Phys. Rev. Lett.* **70**, 2952 (1993).
 - ¹⁷ See Supplemental Material at [URL will be inserted by publisher] for derivations of the effect of noise on the reconstructed phase.
 - ¹⁸ J. F. Annett, *Superconductivity, Superfluids and Condensates* (Oxford University Press, Oxford, 2004).
 - ¹⁹ J. Karpinski, S. M. Kazakov, J. Jun, M. Angst, R. Puzniak, A. Wisniewski, and P. Bordet, *Physica C* **385**, 42 (2003).
 - ²⁰ D. B. Williams and C. B. Carter, *Transmission Electron Microscopy* (Springer, New York, 1996) Chap. 28.
 - ²¹ R. F. Egerton, *Rep. Prog. Phys.* **72**, 016502 (2009).
 - ²² D. Rez, P. Rez, and I. Grant, *Acta. Cryst.* **A50**, 481 (1994).
 - ²³ J. R. Clem, *J. Low Temp. Phys.* **18**, 427 (1975).
 - ²⁴ M. Beleggia and G. Pozzi, *Phys. Rev. B* **63**, 054507 (2001).
 - ²⁵ W. H. Press, B. P. Flannery, S. A. Teukolsky, and T. T. Vetterling, *Numerical Recipes* (Cambridge University Press, Cambridge, 1992) Chap. 10.4.
 - ²⁶ A. C. Twitchett, R. E. Dunin-Borkowski, and P. A. Midgley, *Phil. Mag.* **86**, 5805 (2006).
 - ²⁷ M. Beleggia, M. A. Schofield, V. V. Volkov, and Y. Zhu, *Ultramicroscopy* **102**, 37 (2004).
 - ²⁸ C.-H. Sow, K. Harada, A. Tonomura, G. Crabtree, and D. G. Grier, *Phys. Rev. Lett.* **80**, 2693 (1998).
 - ²⁹ E. Völkl, L. Allard, and D. Joy, eds., *Introduction to Electron Holography* (Kluwer Academic, New York, 1999).
 - ³⁰ H. Lichte, K.-H. Herrmann, and F. Lenz, *Optik* **77**, 135 (1987).